Determination of the thermoelectric properties of a skutterudite-based device at practical operating temperatures by impedance spectroscopy

Chung-Yul Yoo[a,*], Changho Yeon[a], Younghwan Jin[a], Yeongseon Kim[a], Jinseop Song[a], Hana Yoon[a], Sang Hyun Park[a], Braulio Beltrán-Pitarch[b], Jorge García-Cañadas[b], Gao Min[c]

[a]Korea Institute of Energy Research, 152 Gajeong-ro, Yuseong-gu, Daejeon 34129, Republic of Korea

[b]Department of Industrial Systems Engineering and Design, Universitat Jaume I, Campus del Riu Sec, 12071 Castellón, Spain

[c]School of Engineering, Cardiff University, Cardiff CF24 3AA, United Kingdom

* To whom all correspondence should be addressed. Tel: +82-42-860-3083, Fax: +82-42-860-3133, E-mail: cyoo@kier.re.kr (Chung-Yul Yoo)

1

Abstract

Skutterudite-based thermoelectric materials are promising candidates for waste heat recovery applications at intermediate temperatures (300–500 °C) owing to their high dimensionless figure of merit and power factor. Recently, several researchers have reported the high performance of skutterudite-based thermoelectric devices obtained by optimizing the crystal structure and microstructure of skutterudite materials and developing metallization layers for device fabrication. Despite extensive research efforts toward maximizing the power density and thermoelectric conversion efficiency of skutterudite-based devices, the thermoelectric properties of such devices after fabrication remain largely unknown. Here, we systematically investigated the factors that affect the thermoelectric properties of skutterudite-based devices within the range of practical operating temperatures (23–450 °C). We successfully prepared a two-couple skutterudite-based device with titanium metallization layers on both sides of the thermoelectric legs and characterized it using scanning and transmission electron microscopy and specific contact resistance measurements. Impedance spectroscopy measurements of the two-couple skutterudite-based device revealed the figure of merit of the device and enabled the extraction of three key thermoelectric parameters (Seebeck coefficient, thermal conductivity, and electrical conductivity). The impedance spectra and extracted parameters depended strongly on the measurement temperature and were mainly attributable to the thermoelectric properties of skutterudite materials. These observations demonstrate the interplay between the properties of thermoelectric materials and devices and can aid in directing future research on thermoelectric device fabrication.

1. Introduction

Owing to the increasing demand for waste heat harvesting technologies, significant advances have been made over the past few decades toward the development of highly efficient bismuth telluride [1–3], germanium telluride [4,5], lead telluride [6,7], skutterudite (SKD) [8–12], half-Heusler [9,13–15], and oxide [9,14] based materials as well as bismuth telluride [16,17], lead telluride [18,19], SKD [20–25], half-Heusler [26–28] based thermoelectric devices. Thermoelectric devices due to their solid-state nature have the advantage of no moving parts and consequently offer compactness, quietness, and high reliability. The thermoelectric conversion efficiency of materials and devices is mainly determined by the figure of merit, $ZT = T\sigma S^2/\lambda$, where T is the absolute temperature, σ the electrical conductivity, S the Seebeck coefficient, and λ the thermal conductivity. To date, most efforts have focused on enhancing the ZT values of thermoelectric materials by optimizing the chemical composition [6,8,10] and microstructure [13,15]. However, it is a significant challenge to determine the thermoelectric properties of devices because of their complex structures, which comprise arrays of thermoelectric legs, metallization layers, electrodes, and insulating plates.

To characterize thermoelectric devices, Harman's method and power output measurements have been widely used to evaluate the ZT values and thermoelectric power, respectively, but additional extensive measurements are necessary to determine the three key parameters (σ, S, and λ). Recently, several studies have demonstrated that impedance spectroscopy can be used to determine the ZT values of thermoelectric bismuth telluride [29] and SKD [30,31] materials as well as bismuth telluride [32–38] and SKD [39,40] based devices. In a typical galvanostatic impedance spectroscopy measurement, a sinusoidal current perturbation

drives the thermoelectric system slightly out of temperature equilibrium (appearance of a temperature gradient), inducing reorganization of the carriers owing to the Peltier effect, which allows the Seebeck voltage to be measured as a function of frequency. The impedance value at a given frequency is obtained from the ratio of the measured voltage amplitude to the applied current amplitude together with the phase angle difference. This protocol is repeated over several decades of frequency to obtain the impedance spectrum. ZT and the three key parameters (σ, S, and λ) can then be extracted using suitable mathematical models (equivalent circuits) [29,37].

Most investigations using impedance spectroscopy for the characterization of bismuth telluride [29,32,34,35,38] and SKD [39,40] based thermoelectric devices have been performed at ambient temperature, with only a few studies reporting the properties of bismuth telluride based devices at operating temperatures up to 150 °C [33,37]. In this work, we employed impedance spectroscopy to elucidate the thermoelectric properties of an in-house-fabricated two-couple SKD-based device within the range of practical operating temperatures (23–450 °C) with the help of state-of-the-art mathematical models along with electrical, thermal, and microstructural characterization. To the best of our knowledge, this is the first detailed and systematic investigation of the factors that affect the properties of SKD-based thermoelectric devices.

2. Materials and methods

2.1 Materials, device fabrication, and electrical/thermal property measurements

Commercial SKD powders (composition $DD_yFe_3CoSb_{12}$ for p-type SKD and $(Mm,Sm)_yCo_4Sb_{12}$ for n-type SKD, where DD and Mm stand for didymium and mischmetal, respectively) were provided by Treibacher Industrie AG [24,41]. The as-received SKD powders

4

(3 g) were sandwiched between two Ti foils (50 μm thickness, Alfa Aesar, 99.6%) and then cold-pressed using a graphite die with a diameter of 12 mm. SKD discs metallized on both sides with Ti (Ti/SKD/Ti joints) were prepared by spark plasma sintering (SPS) (SPS-211LX, Fuji Electronic Industrial Co., Ltd.) at 620 °C for p-type SKD and 650 °C for n-type SKD at 50 MPa under 1.3×10^{-4} kPa. To fabricate a two-couple device, cube-shaped legs with sizes of $4 \times 4 \times 4$ mm^3 were cut from the sintered discs and polished using 1 μm grade alumina abrasive. The two p-type and n-type SKD legs were integrated in series with Cu electrodes on an Al_2O_3 substrate (thickness 0.76 mm) using an Incusil-series brazing alloy on both sides. Conductive Ag paste was used to connect four copper wires to the SKD device, and then the joint was covered using graphite paste to ensure connection between the SKD device and the wires, as shown in Fig. 1 (a). Fig. 1 (b) shows that similar impedance spectra are obtained for the wireless SKD device suspended in a vacuum chamber and the wired SKD device in a heating block with an insulating cloth. It can been seen from Fig. 1 (b) that the resistance of the wires in the thermoelectric device is less than 10 μΩ; hence, the wiring, insulating cloth, and heating block have insignificant effects on the impedance spectroscopy measurements.
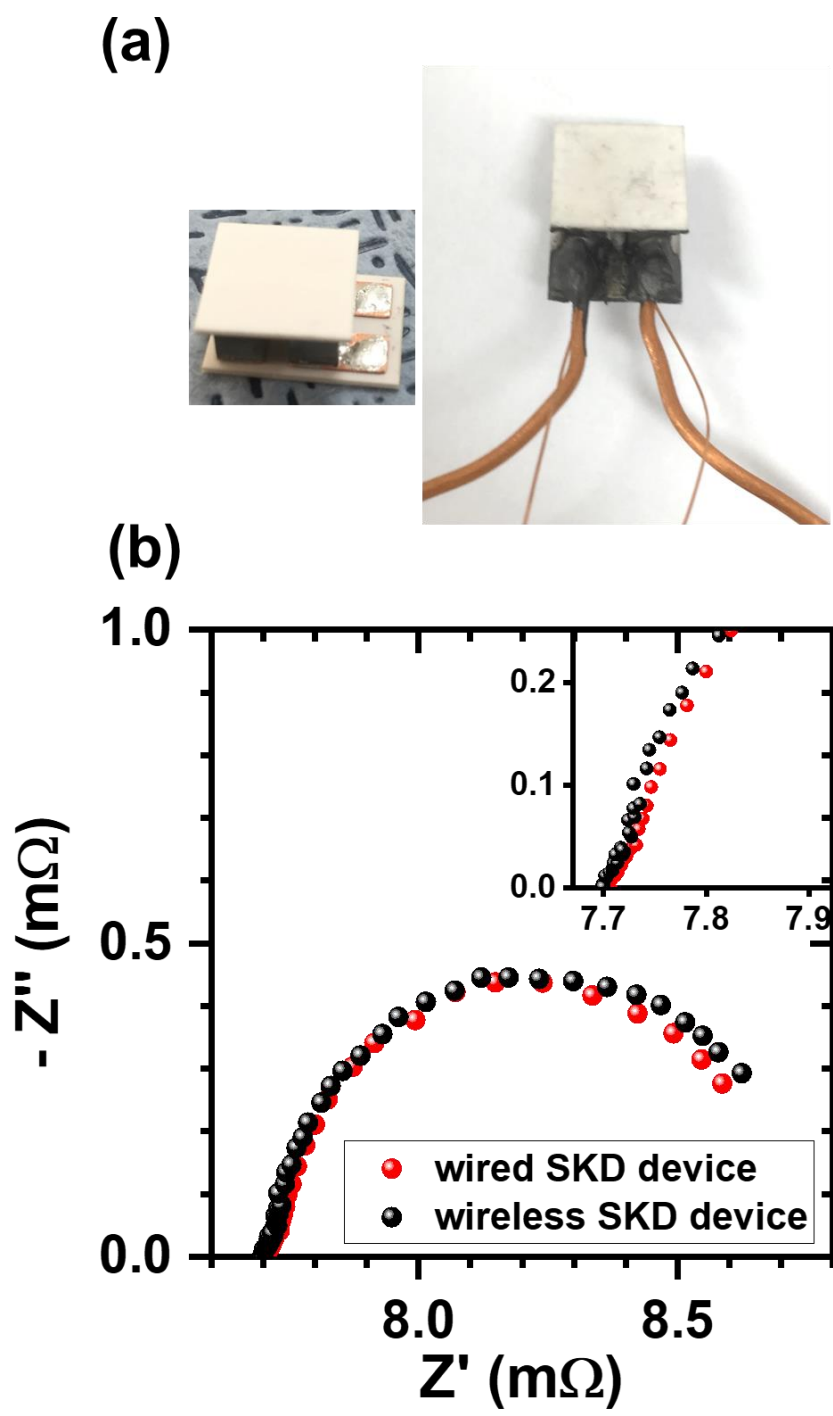
Fig. 1 (a) Photographs of the wireless and wired two-couple SKD device. (b) Impedance spectra of the wireless SKD device suspended in a vacuum chamber and the wired SKD device in a heating block with an insulating cloth.

The interface between Ti and SKD (Ti/SKD) was examined using scanning electron microscopy (SEM) together with energy-dispersive X-ray spectroscopy (EDS) (JEOL JSM-7000F). The details of the Ti/SKD interfacial structure were investigated by high-angle annular dark-field scanning transmission electron microscopy (HAADF-STEM) (JEOL JEM-2100F and JEM-ARM200) together with EDS and selected-area electron diffraction (SAED). The lamellar specimens were prepared using a focused ion beams (FIB) (Helios NanoLab). The SAED patterns were analyzed using the CrysTBox software [42]. The specific contact resistance at the Ti/SKD interface was evaluated using an in-house electrical contact resistivity apparatus at 23 °C [43]. Laser flash analysis (LFA 447, Netzsch) was employed to measure the thermal diffusivity of the SKD materials and Al_2O_3 substrate. The thermal conductivity was obtained as $\lambda_{TE} = D \cdot C_p \cdot \rho$, where D is the thermal diffusivity, C_p is the specific heat, and ρ is the mass density of the specimen. The temperature-dependent C_p values were measured directly using differential scanning calorimetry (DSC 214 Polyma, Netzsch). The ρ values were determined from mass and volume measurements for each specimen.

2.2 Impedance spectroscopy measurements and data analysis

The SKD device was suspended in a vacuum chamber (0.13 kPa) and placed in a copper heating block. To avoid direct contact between the thermoelectric device and the copper heating block, the interface was insulated using multiple layers of ceramic insulation cloth (RS-Cloth, Zircar Inc.). A schematic of the experimental setup is shown in Fig. S1 in the Supplementary Material. The impedance spectroscopy data for the SKD device were collected over the temperature range of 23–450 °C in the frequency range of 10^{-2} to 10^3 Hz using a

potentiostat/galvanostat (Autolab PGSTAT302N, Metrohm) connected to a 10 A current booster

with a sine-wave oscillation current in a four-probe configuration. In a previous study by our

group [40], it was found that the oscillation current value corresponding to the Peltier heat power

density of 1000 W·m^{-2} for an SKD two-couple thermoelectric device was in good agreement

with the results of Beltrán-Pitarch $et\ al.$ [30]. As the S values of SKD materials increase with

temperature, the Peltier power density was employed to optimize the oscillation current

amplitude value at each temperature. The optimized current amplitude (I) at each measurement

temperature was calculated using $I = PP(A/(S_{ave}T))$, where PP is the Peltier power density

(1000 W·m^{-2}), S_{ave} is the average Seebeck coefficient for p-type and n-type SKD at each

temperature [24], T is the absolute temperature, and A is the area of the thermoelectric legs. At

each measurement temperature, the isothermal condition was assumed for the impedance

spectroscopy measurements when there was no change in the recorded impedance spectra.

The obtained impedance spectra were analyzed using both i) ideal [29] and ii)

comprehensive [37] models to characterize the thermoelectric device properties. The ideal model

is derived from a one-dimensional heat equation, as described by García-Cañadas and Min [29]

under the assumption of adiabatic conditions in all surfaces. It can be written as,

$$Z(j\omega) = R_\Omega + \left(\frac{1}{Z_{WCT}(j\omega)^{-1} + Z_{Wa}(j\omega)^{-1}}\right), \tag{1}$$

where R_Ω is the total ohmic resistance, $j = (-1)^{0.5}$, and ω is the angular frequency. Z_{WCT} and Z_{Wa}

are a constant temperature Warburg element and an adiabatic Warburg element, respectively,

which are defined as:

$$Z_{\text{WCT}}(j\omega) = R_{\text{TE}} \left(\frac{j\omega}{\omega_{\text{TE}}}\right)^{-0.5} \tanh\left[\left(\frac{j\omega}{\omega_{\text{TE}}}\right)^{0.5}\right], \tag{2}$$

$$Z_{\text{Wa}}(j\omega) = R_{\text{C}} \left(\frac{j\omega}{\omega_{\text{C}}}\right)^{-0.5} \coth\left[\left(\frac{j\omega}{\omega_{\text{C}}}\right)^{0.5}\right], \tag{3}$$

where $R_{\text{TE}} = 2NS^2TL/(\lambda_{\text{TE}}A)$ is the thermoelectric resistance and $R_{\text{C}} = 4NS^2TL_{\text{C}}/(\lambda_{\text{C}}A)$ is the thermoelectric resistance induced by the ceramic layer. In addition, $\omega_{\text{TE}} = \alpha_{\text{TE}}/(L/2)^2$ and $\omega_{\text{C}} = \alpha_{\text{C}}/L_{\text{C}}^2$ are the characteristic angular frequencies of thermal diffusion for the thermoelectric and ceramic materials, respectively, where N is the number of thermoelectric couples, T is the absolute temperature, λ_{TE} and λ_{C} are the thermal conductivities of the thermoelectric element and insulating ceramic plate, respectively, L and L_{C} are the lengths of the thermoelectric element and ceramic plate, respectively, and α_{TE} and α_{C} are the thermal diffusivities of the thermoelectric element and ceramic plate, respectively.

The σ, S, λ_{TE}, and ZT values can be calculated using the following expressions:

$$\sigma = 2N\frac{L}{R_\Omega A}, \tag{4}$$

$$S = \sqrt{\frac{R_{\text{C}}\lambda_{\text{C}}A}{4NTL_{\text{C}}}}, \tag{5}$$

$$\lambda_{\text{TE}} = \frac{2NS^2TL}{R_{\text{TE}}A}, \tag{6}$$

$$ZT = \frac{S^2\sigma}{\lambda_{\text{TE}}}T = \frac{R_{TE}}{R_\Omega}, \tag{7}$$

where the parasitic contributions to the ohmic resistance (wires, copper strips, and electrical contacts between them) are neglected.

To estimate the thermoelectric parameters accurately, a more comprehensive model can be derived from a corrected one-dimensional heat equation including thermal convection, radiation, and spreading-constriction thermal impedance corrections, as described by Mesalam *et al.* [37]:

$$Z_{\mathrm{m}}(\mathrm{j}\omega) = R_\Omega + \left(\frac{1}{Z_{\mathrm{WTE,m}}(\mathrm{j}\omega)^{-1}+Z_{\mathrm{Wa,m}}(\mathrm{j}\omega)^{-1}}\right), \tag{8}$$

where the modified constant temperature Warburg element and adiabatic Warburg take the following forms:

$$Z_{\mathrm{WTE,m}}(\mathrm{j}\omega) = R_{\mathrm{TE}} \left(\frac{h_1 L^2}{2\lambda_{\mathrm{TE}} r_0} + \frac{\mathrm{j}\omega}{\omega_{\mathrm{TE}}}\right)^{-0.5} \tanh\left[\left(\frac{h_1 L^2}{2\lambda_{\mathrm{TE}} r_0} + \frac{\mathrm{j}\omega}{\omega_{\mathrm{TE}}}\right)^{0.5}\right], \tag{9}$$

$$
\begin{aligned}
Z_{\mathrm{Wa,m}}(\mathrm{j}\omega) = \Bigg\{ & \left(\frac{4NS^2 T}{h_2 A}\left(\frac{\eta}{1-\eta}\right)\right)^{-1} \\
& + \Bigg[\frac{4NS^2 T}{Y_{\mathrm{SC}} A} \\
& + \left(\left(\frac{4NS^2 T}{h_3 A}\right)^{-1} + \left(\eta R_{\mathrm{C}}\left(\frac{\mathrm{j}\omega}{\omega_{\mathrm{C}}}\right)^{-0.5}\coth\left[\left(\frac{\mathrm{j}\omega}{\omega_{\mathrm{C}}}\right)^{0.5}\right]\right)^{-1}\right)^{-1} \\
& + \left(\left(\eta R_{\mathrm{C}}\left(\frac{\mathrm{j}\omega}{\omega_{\mathrm{C}}}\right)^{-0.5}\tanh\left[\left(\frac{\mathrm{j}\omega}{\omega_{\mathrm{C}}}\right)^{0.5}\right]\right)^{-1} \\
& + \left(\frac{4NS^2 T L_{\mathrm{C}}^2 h_3 \omega_{\mathrm{C}}}{\mathrm{j}\omega A \lambda_{\mathrm{C}}^2 \eta^2}\right)^{-1}\right)^{-1}\Bigg]^{-1}\Bigg\}^{-1},
\end{aligned}
\tag{10}
$$

where η is the filling factor (0.66), r_0 is the thermoelectric leg radius ($\sqrt{A/\pi}$), Y_{SC} is the

spreading-constriction impedance between the SKD legs and the Al_2O_3 plate (given by

$$\frac{1}{Y_{SC}} = \frac{4L_C}{\lambda_C} \sum_{n=1}^{\infty} \left[\frac{J_1^2(\delta_n \eta^{0.5})\coth(\eta\delta_n^{\;2}(\frac{\pi L_C^2}{A}) + \frac{j\omega}{\omega_C})^{0.5})}{\delta_n^{\;2}J_0^2\delta_n\left(\eta\delta_n^{\;2}\left(\frac{\pi L_C^2}{A}\right) + \frac{j\omega}{\omega_C}\right)^{0.5}} \right],$$

in which J_0 and J_1 are the zero- and first-order Bessel functions of the first kind, and δ_n is the nth

zero root of J_1), σ_B is the Stefan–Boltzmann constant (5.67×10^{-8} kg·s^{-3}·K^{-4}), ε is the emissivity

(0.9 for SKD [44] and 0.5 for Al_2O_3 [37]), $h_1 = 4\sigma_B\varepsilon_{TE}T^3$ is the radiative heat loss of the

thermoelectric legs, $h_2 = 4\sigma_B\varepsilon_C T^3$ is the radiative heat loss at the internal surface of the Al_2O_3

plate, and $h_3 = h_C + 4\sigma_B\varepsilon_C T^3$ is the radiative and convective heat loss at the external surface of

the Al_2O_3 plate (where h_C is the convective heat transfer coefficient at the external surface of the

ceramic plates. The σ, S, λ_{TE}, and ZT values were calculated using Eq. (4)–(7). For both the

models, the complex nonlinear least-squares analysis of the impedance spectra was performed

with MATLAB using five free fitting variables (R_Ω, R_C, R_{TE}, ω_C, and ω_{TE}) simultaneously by

minimizing a functional that measures the discrepancies between the obtained data and the

models. The fittings of the experimental data to the above equations were carried out using the

built-in function "lsqcurvefit" from the MATLAB Optimization Toolbox with a trust-region

reflective algorithm and convergence criteria (80,000 iterations, tolerance 10^{-15}).

## 3. Results and discussion

The Ti metallization layer has been found to exhibit a low specific contact resistance and

excellent bonding characteristics for SKD-based thermoelectric materials ($CoSb_3$ [45–47],

$Yb_{0.6}Co_4Sb_{12}$ [48], and $Ce_yFe_xCo_{4-x}Sb_{12}$ [49]). Fig. 2 shows the cross-sectional SEM images and EDS elemental line-scan results for the Ti/SKD interfaces, together with the specific contact resistance between Ti and SKD. As shown in the SEM images in Fig. 2a and c, the metallization layers are tightly bonded to the SKD leg surfaces. However, the EDS line-scan results indicate that some intermetallic phases are formed during SPS because of the interfacial reaction at the Ti/SKD interface. To perform a more detailed analysis, HAADF-STEM images and SAED patterns were obtained from the FIB lamella prepared from the Ti/SKD interface. The distinct areas of the HAADF-STEM images obtained by contrast difference are shown in Fig. 3a and g for p-type and n-type SKD, respectively. The SAED patterns along the zone axes of the corresponding areas are shown in Fig. 3b–f and h–l and include representative Miller indices. Two intermetallic phases with different crystal structures are observed for Ti/p-type SKD, namely, hexagonal TiSb near Ti and orthorhombic $(FeCo)Sb_2$ near p-type SKD. In contrast, three intermetallic phases are observed for Ti/n-type SKD, namely, hexagonal TiSb near Ti, and orthorhombic $CoSb_2$ and cubic TiCoSb near n-type SKD. These observations are consistent with the SEM-EDS results. Moreover, the observation of intermetallic compounds at the Ti/SKD interface is in good agreement with the results reported in the literature [45,46,48–50]. Detailed indexing of the SAED patterns is provided in the Supplementary Material (Fig. S2 and S3). According to previous reports [45,46,48,49], the formation and growth of TiSb and TiCoSb phases are further accelerated upon heat treatment at temperatures above 500 °C, resulting in an increase in the electrical contact resistance and fracture failure of Ti/SKD interfaces. Hence, in this study, the impedance spectroscopy measurements of the SKD device were only performed up to 450 °C to avoid the formation of further TiSb and TiCoSb phases. Even though there is an interfacial reaction between Ti and SKD, the specific contact resistivity at the Ti/SKD interface

was very low (3.06 $\mu\Omega \cdot cm^2$ for p-type SKD and 4.37 $\mu\Omega \cdot cm^2$ for n-type SKD), in agreement with previous studies [48,49].
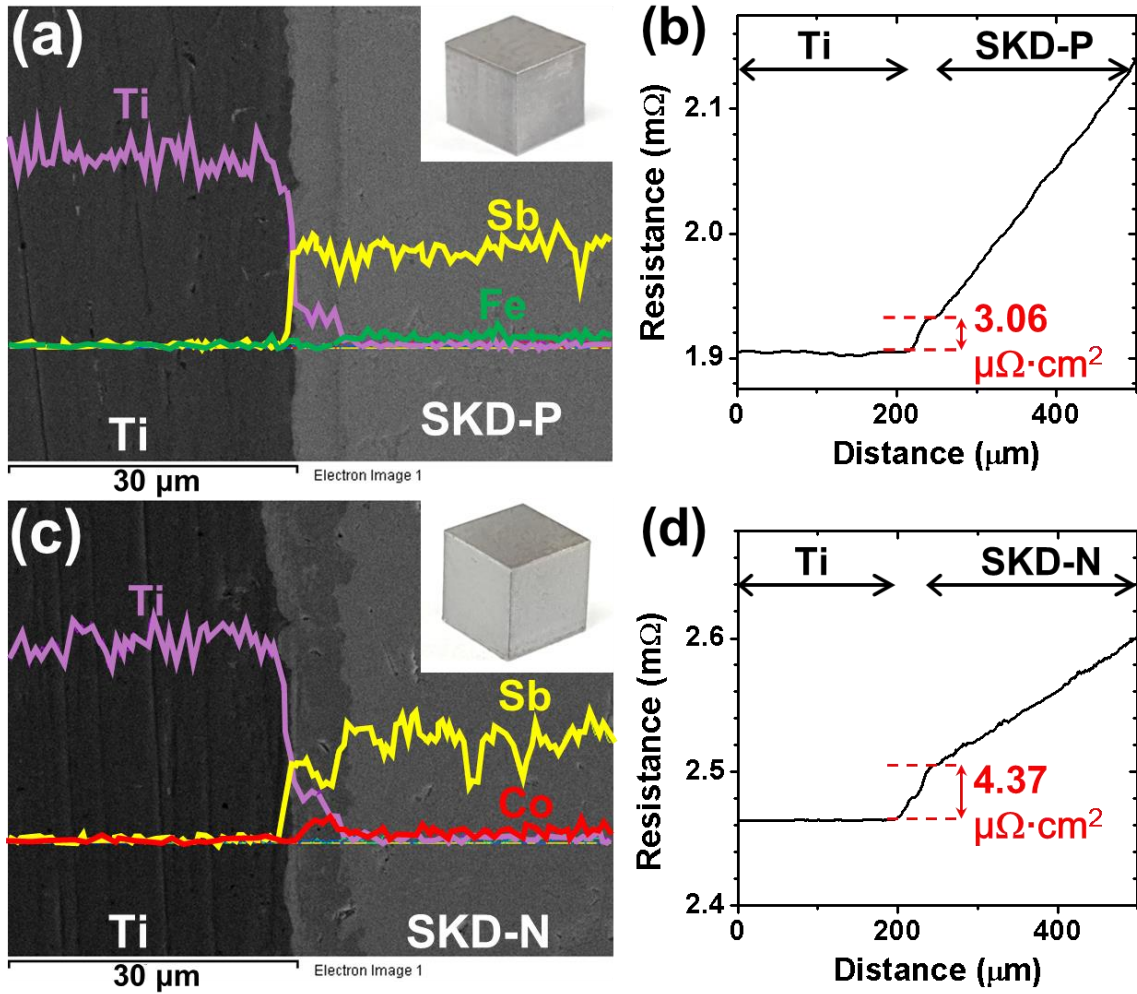

Fig. 2 Scanning electron microscopy (SEM) images with energy-dispersive X-ray spectroscopy (EDS) line scanning profiles (left) and electrical contact resistivity (right) of Ti metallized (a, b) p-type skutterudite (SKD) joints and (c, d) n-type SKD joints. Insets: photographs of the Ti metallized SKD thermoelectric legs.
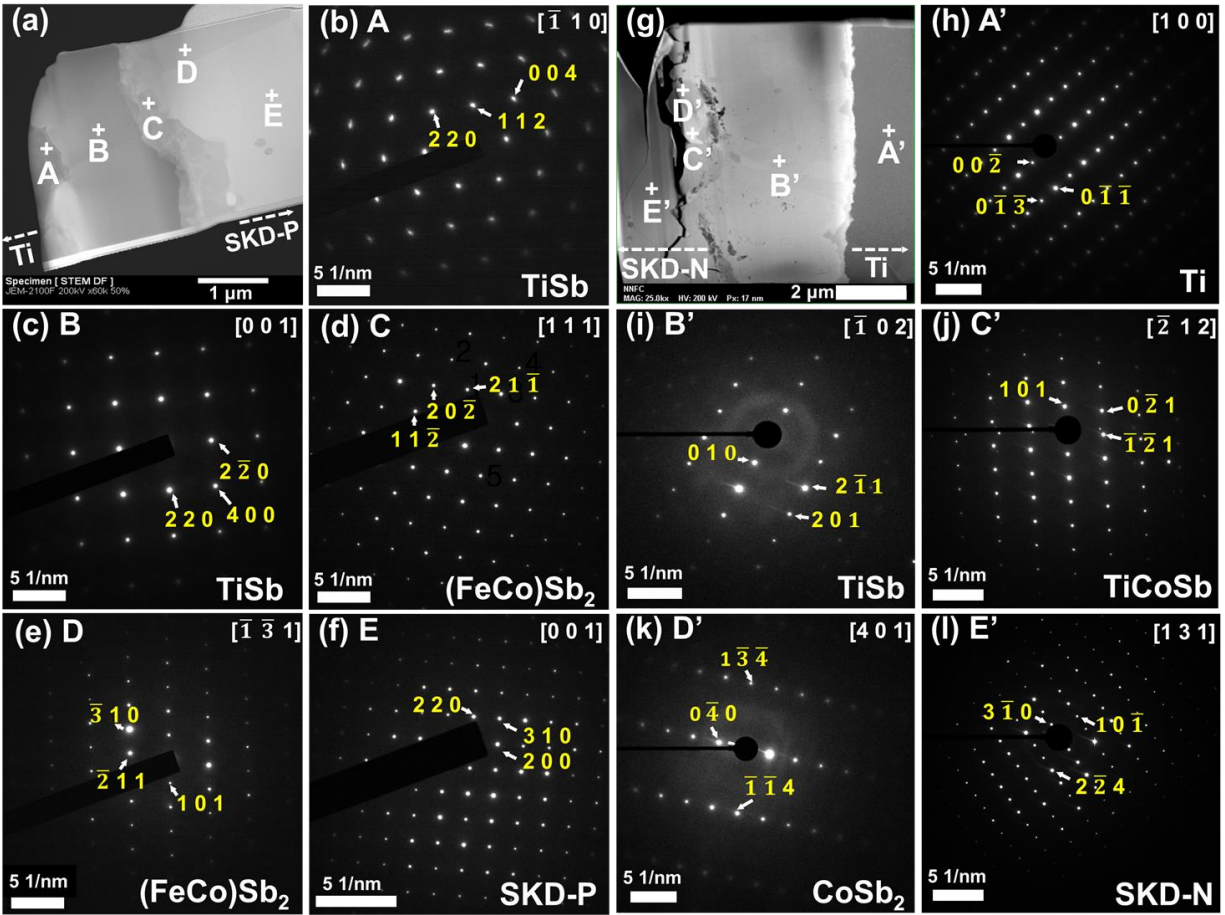
Fig. 3 High-angle annular dark-field scanning transmission electron microscopy (HAADF-STEM) images at the Ti/SKD interface and selected-area electron diffraction (SAED) patterns of the corresponding regions in the HAADF-STEM images along the [*u v w*] zone axis for (a–f) p-type SKD and (g–l) n-type SKD.

Prior to the detailed analysis, Kramers–Kronig (KK) transformation tests were performed to evaluate the impedance spectra of the SKD device. This method provides a very effective way to assess the consistency of spectra and to exclude spectra containing non-steady-state behavior in the field of thermoelectrics [40], solid state ionics [51,52], and electrochemistry [53]. As shown in Fig. 4, to validate the measurements, residual plots for the deviations of the real ($\Delta Z_{re}(\omega)$) and imaginary ($\Delta Z_{im}(\omega)$) parts can be obtained from the differences between the experimental impedance data (Z_{re} and Z_{im}) and the KK transformation results ($Z_{re,KK}$ and $Z_{im,KK}$). The impedance spectra at frequencies higher than 0.2 Hz are mainly due to the contacts (electrical contacts and Al_2O_3 plates); hence, the observation of residual errors close to zero at frequencies higher than 0.2 Hz indicates that the in-house-fabricated two-couple SKD device has excellent contact characteristics. At frequencies lower than 0.2 Hz, the residual errors are higher (up to 0.4%) and increase slightly with temperature. The impedance spectra at frequencies lower than 0.2 Hz are related to the Seebeck voltage of both p-type and n-type SKD thermoelectric materials. The high residual errors at frequencies lower than 0.2 Hz could originate from the heat loss of the thermoelectric legs upon Peltier heating/cooling during impedance spectroscopy measurements. Nevertheless, as the residual errors are less than $\pm 0.5\%$ over the entire frequency range [40,53], all of the impedance spectra of the SKD device are a response to the current oscillation applied under the steady-state conditions. Therefore, all of the impedance spectra are KK-transformable and can be further analyzed by nonlinear least-squares analysis to evaluate the thermoelectric properties of the two-couple SKD device.

15
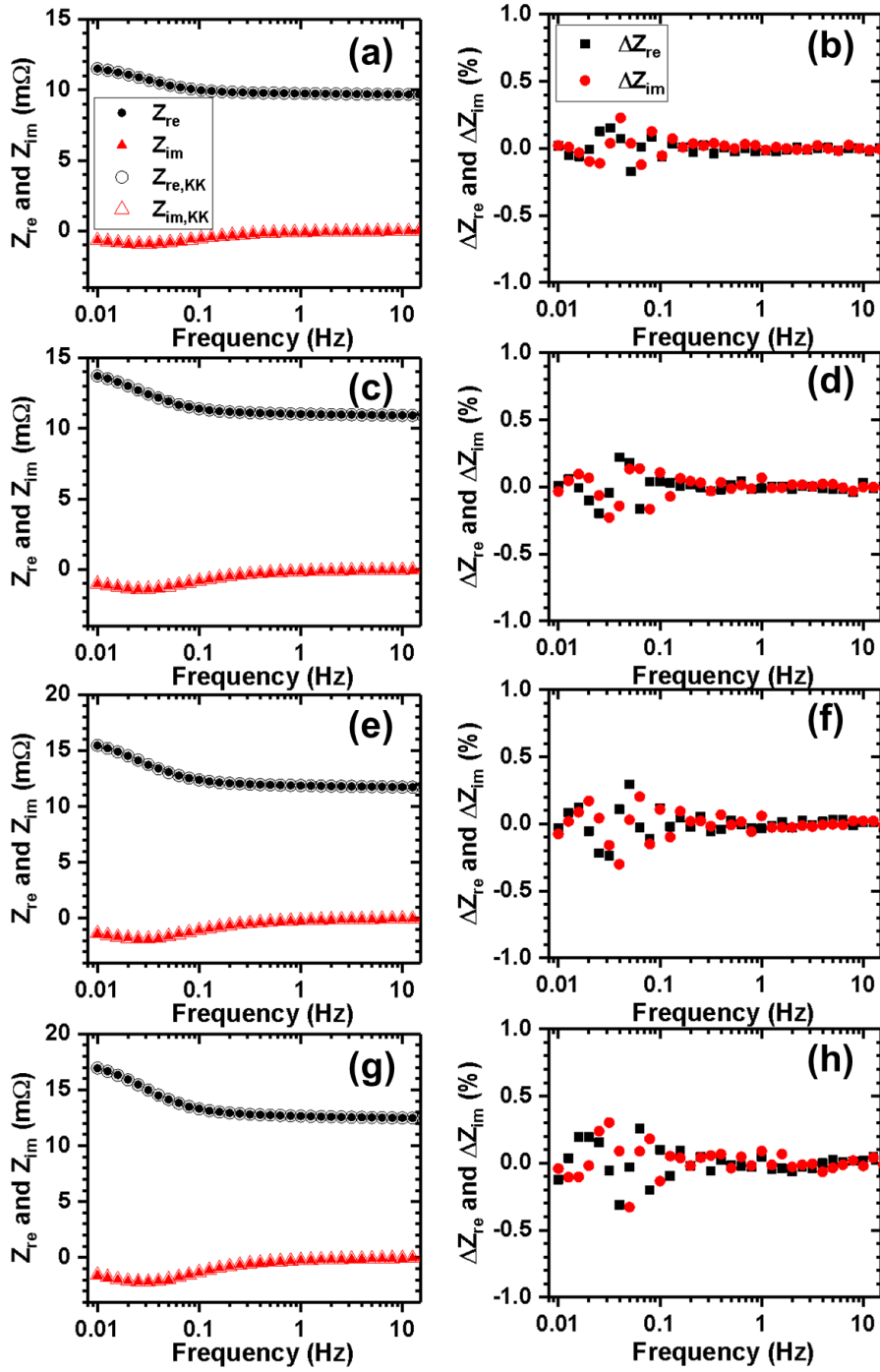
Fig. 4 Kramers–Kronig (KK) transformation results (empty symbols) of impedance spectra (filled symbols) (left) and residual plots (right) for the two-couple SKD device at (a, b) 150 °C, (c, d) 250 °C, (e, f) 350 °C, and (g, h) 450 °C.

Fig. 5 shows the Nyquist plots of the impedance spectra for the two-couple SKD device over the temperature range 23–450 °C. The high-frequency real axis intercept of each impedance spectrum corresponds to the ohmic electrical resistance of the SKD device, which increases with temperature, mainly because of the increase in the electrical resistance of the SKD thermoelectric materials. From this point towards lower frequencies, a linear trend overlapped with an impedance arc is observed due to the response of the Al_2O_3 insulating plates and thermoelectric materials integrated in the SKD device upon application of current perturbation. The contribution of the arc increases with temperature, mainly owing to the increase in $ZT \cdot \sigma^{-1}$ of the SKD thermoelectric materials with temperature.
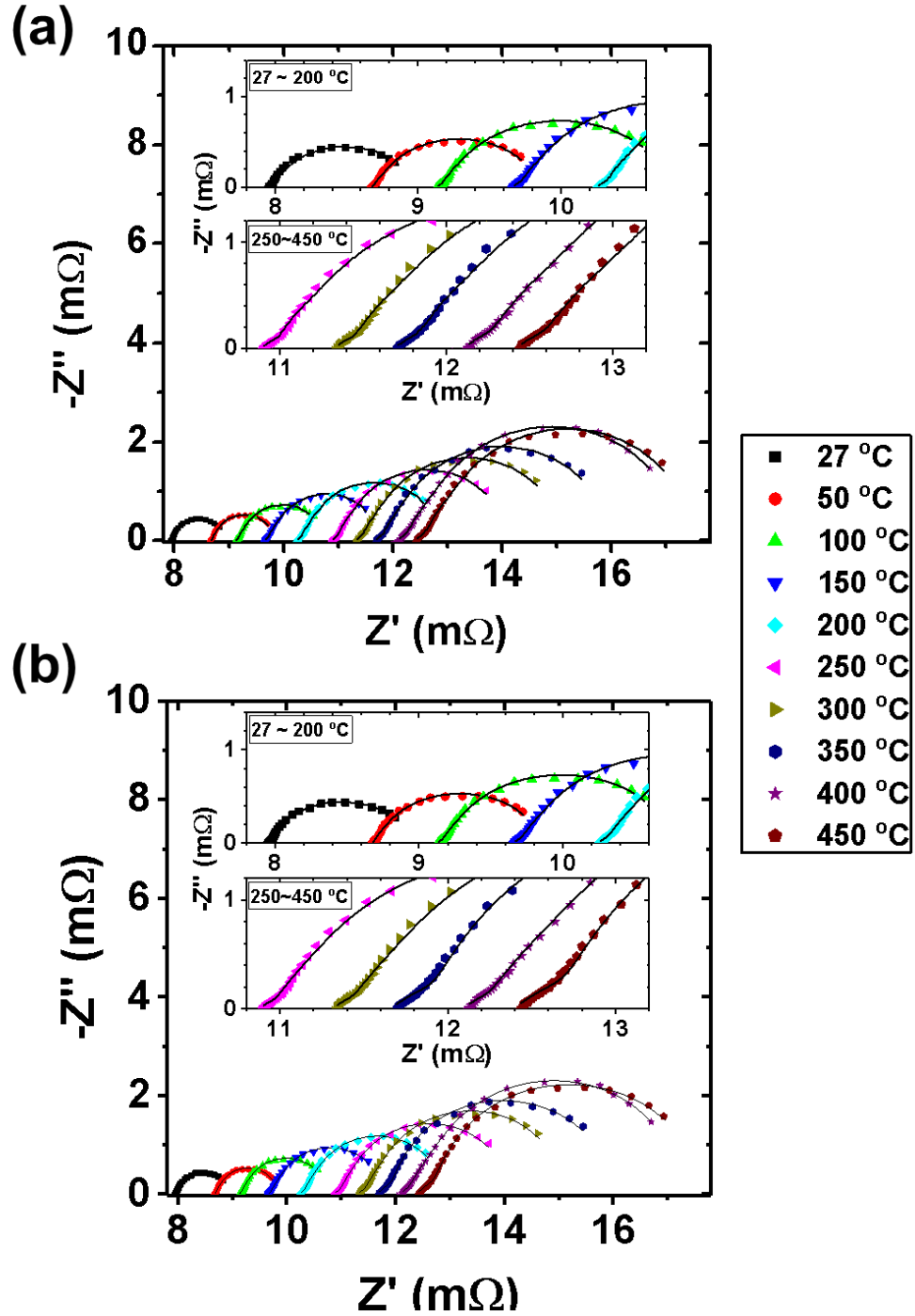
Fig. 5 Impedance spectra of the two-couple SKD device at various temperatures (filled symbols) and mathematical model fitting results (lines) using the (a) ideal and (b) comprehensive models.

The obtained spectra were analyzed using both the ideal and the comprehensive models. Both models require five fitting parameters (R_Ω, R_C, R_{TE}, ω_C, and ω_{TE}) to describe the spectrum obtained at each temperature when the thermal conductivity of the Al_2O_3 plate (λ_C) is known at each temperature. Considerable care must be taken to use an appropriate value for λ_C, as it is used to obtain the S values and, then, the λ_{TE} values. Fig. 6 shows λ_C as a function of temperature, as determined using differential scanning calorimetry and laser flash analysis results. As shown in Fig. 6, λ_C decreases by 50% with the increase in temperature; hence, it is necessary to measure the thermal conductivity of the insulating plate of the thermoelectric device to realize accurate determination of the thermoelectric properties from the impedance spectra of the two-couple SKD device. For the comprehensive model, the convective heat transfer coefficient (h_C) value at the external surface of the Al_2O_3 plate at each temperature is required. At room temperature, a minimum value of 25 $W \cdot m^{-2} \cdot K^{-1}$ obtained a reasonable fitting between the experimental and simulated data, whereas the R_C values were overestimated when the h_C value was less than 25 $W \cdot m^{-2} \cdot K^{-1}$. We explored varying the h_C values to investigate the effect of h_C on the R_C values. The R_C values were found to be within the error range given by nonlinear least-squares fitting analysis at other temperatures when h_C was within the range 25 ± 15 $W \cdot m^{-2} \cdot K^{-1}$. It has been reported that typical heat transfer coefficient values for natural convection at ambient pressure are in the range of 2–25 $W \cdot m^{-2} \cdot K^{-1}$ [54]. The somewhat high heat transfer coefficient value at the external surface of the Al_2O_3 plate may possibly be explained by convective contributions from other parts of the SKD device. Even though the h_C value is somewhat higher than expected at this experimental pressure, the impact of h_C on the ZT value of the device is insignificant (less than 6%) [54] and within the fitting error in this study. Therefore, we used 25 $W \cdot m^{-2} \cdot K^{-1}$ as the h_C value when performing the comprehensive model analysis.
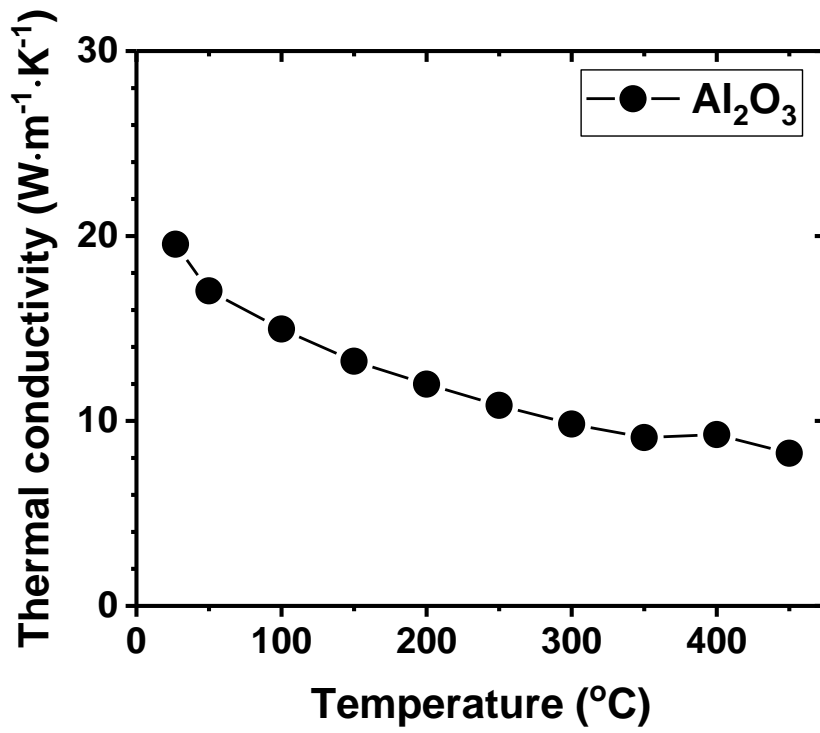
Fig. 6 Thermal conductivity of the Al_2O_3 insulating plate (λ_C) in the two-couple SKD device as a function of temperature.

Fig. 7 shows the values obtained for the five fitting parameters (R_Ω, R_C, R_{TE}, ω_C, and ω_{TE}) as functions of temperature in the range 23–450 °C. The error bars represent the computed standard error of each parameter obtained from the converged fitting procedure. All the resistances (R_Ω, R_C, and R_{TE}) increased with increasing temperature, whereas the angular frequencies (ω_C and ω_{TE}) were found to decrease. The increase in R_Ω is due to the increase in the overall ohmic resistance of the device, whereas the increase in R_{TE} is mainly due to the increase of the Seebeck voltage of the SKD thermoelectric materials. The angular frequencies, ω_C and ω_{TE}, are directly proportional to the thermal diffusivity of the Al_2O_3 plate and SKD materials, respectively. The thermal diffusivity of the Al_2O_3 plate decreased by ~30% with the increase in temperature, whereas that of SKD showed a negligible temperature dependence. Hence, the observed trends for ω_C and ω_{TE} reflect the thermal diffusivity trends of the Al_2O_3 plate and SKD materials. The most pronounced change was observed for the R_C value, which increased from ~0.1 mΩ at 23 °C to ~1.5 mΩ at 450 °C. Using the comprehensive model, the R_C value at 450 °C was approximately 15 times greater than the value at 23 °C; hence, the R_C of the SKD device contributes more than 20% of the overall electrical resistance of the device at 450 °C, but less than 8% at 23 °C.
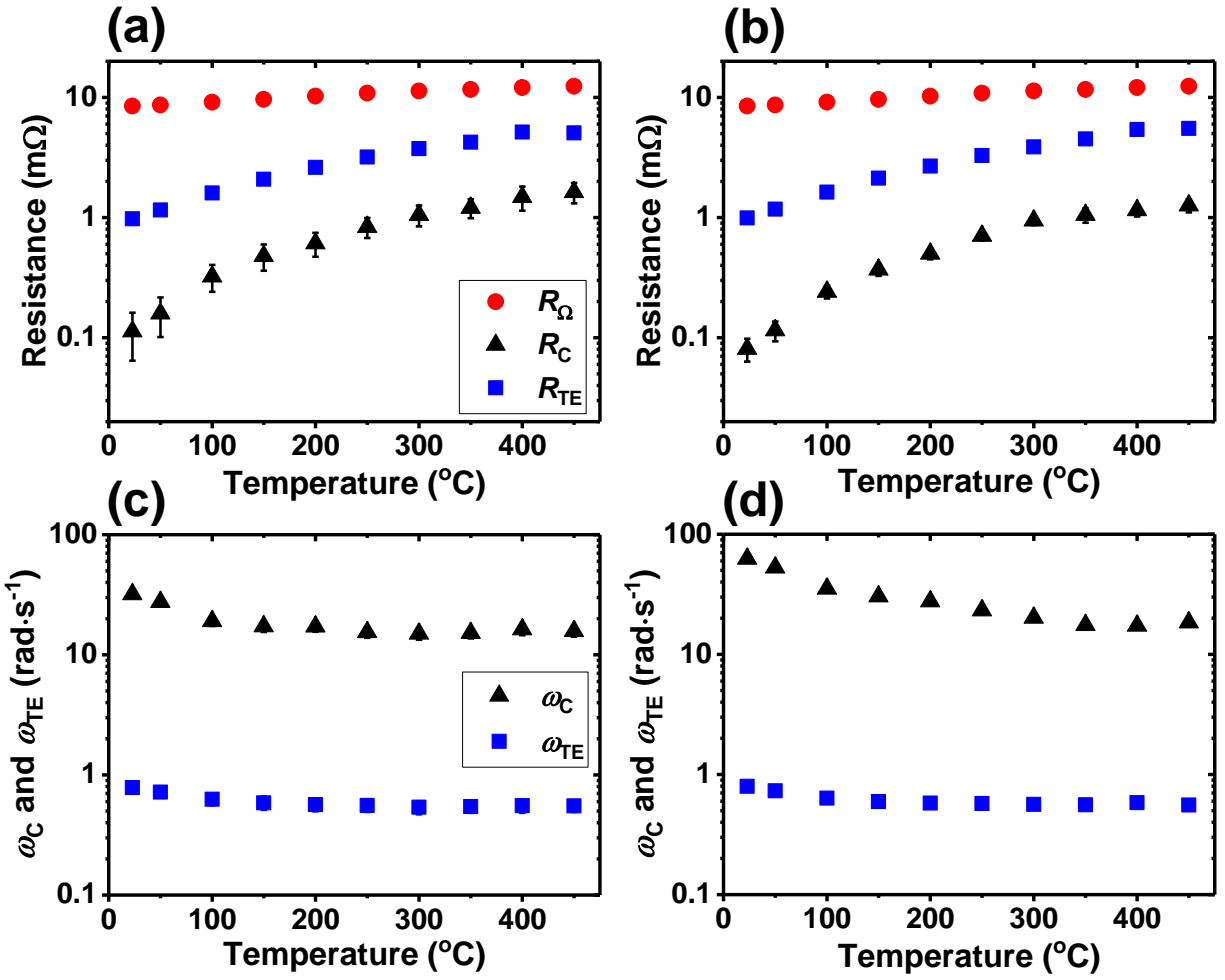
Fig. 7 Variations in the resistance (R_Ω, R_C, and R_{TE}) and angular frequency (ω_C and ω_{TE}) values extracted from the (a, c) ideal and (b, d) comprehensive models as functions of temperature. The error bars represent the standard errors of the complex nonlinear least-squares fitting; where bars are not shown, they are smaller than the symbol size.

To assess the λ_{TE}, σ, S, and ZT values of the SKD device, the three resistances (R_Ω, R_C, and R_{TE}) must be accurately obtained from the fitting. As the fitting error of R_Ω is less than 0.1% of its fitted value, we have constructed error maps in the R_C and R_{TE} plane for the values obtained by fitting the impedance spectra at 150, 250, 350, and 450 °C to the comprehensive model. The goodness-of-fit parameter χ^2 was introduced to assess the quality of fitting: $\chi^2 = \sum_{k=1}^{n}((g_k - g_{m,k})/g_k)$, where g_k and $g_{m,k}$ represent the experimental data obtained and the fitted values predicted by the model, respectively. χ^2 values were calculated for a 100×100 grid around the fitted R_C and R_{TE} values to demonstrate the effect of both R_C and R_{TE} on χ^2. Fig. 8 shows the error maps of the fitting results, confirming that an absolute maximum for reciprocal χ^2 of greater than 500 ($\chi^2 \leq 0.002$) can be obtained for the fitted R_C and R_{TE} values, signifying the reliability of the fitting in this study.
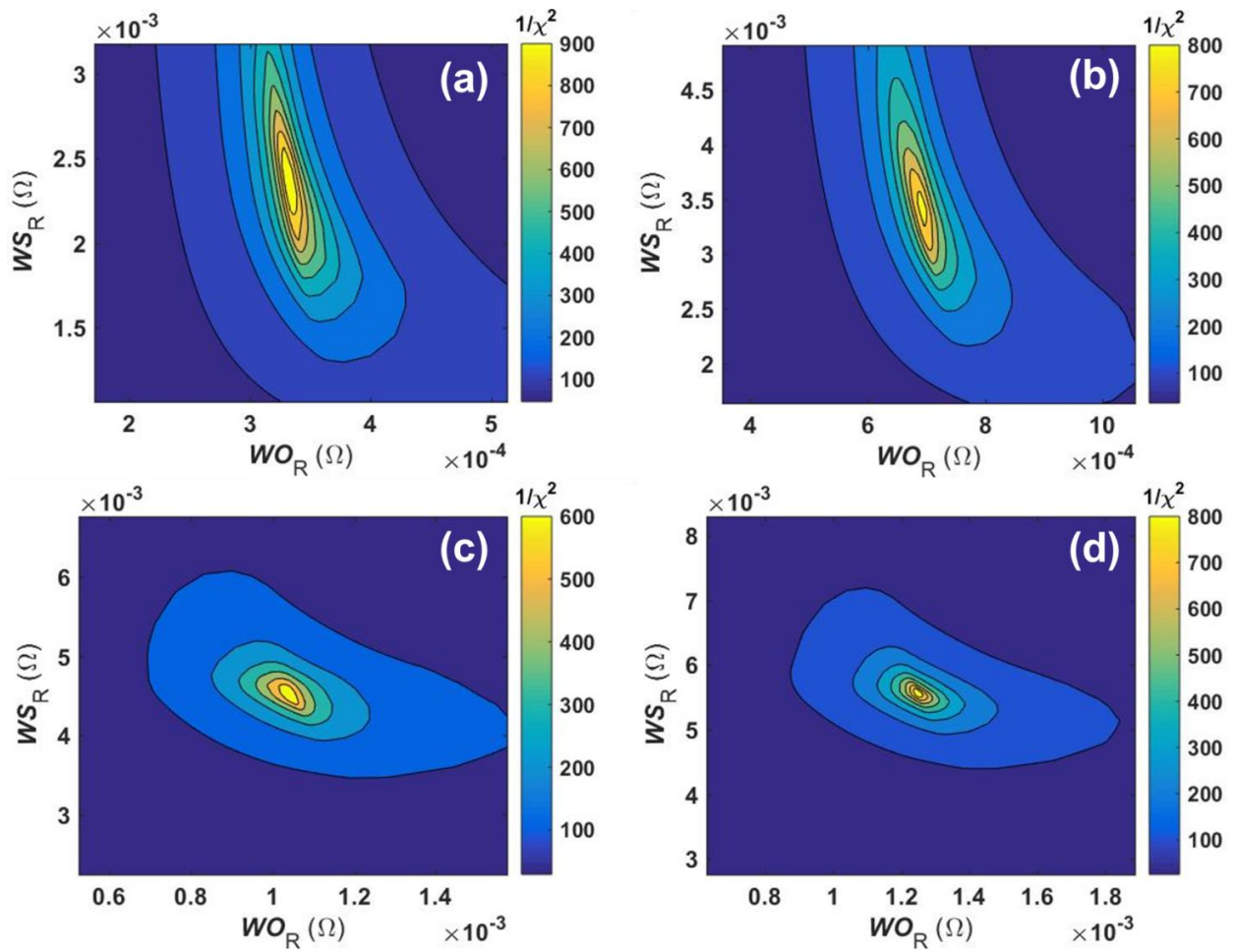
Fig. 8 Fitting error plots showing the values of reciprocal χ^2 calculated for 100×100 grid around the fitted R_C and R_{TE} values. The highest value of χ^{-2} at the center of the plot indicates the lowest deviation of the fitted values from the values obtained at (a) 150 °C, (b) 250 °C, (c) 350 °C, and (d) 450 °C.

Fig. 9 shows the S, λ_{TE}, σ, and ZT values of the SKD device as a function of temperature, as obtained from the impedance spectra using both the ideal and the comprehensive models. The values measured for p-type and n-type SKD materials using ZEM-3 (Ulvac-Riko) and laser flash analysis (LFA 457, Netzsch) [24] are also given for comparison. It can be seen that the S and λ_{TE} values from the comprehensive model show better agreement than those from the ideal model, whereas the σ and ZT values from both models are similar. Therefore, it can be concluded that a model that considers thermal convection, radiation, and spreading-constriction thermal impedance corrections will afford more accurate estimations of S and λ_{TE} than the adiabatic ideal model. It was found that σ decreases with increasing temperature, whereas S increases with increasing temperature. λ_{TE} increases until 300 °C, and then tends to decrease until 450 °C. The σ values obtained for the SKD device are approximately 20% lower than average values for p-type and n-type SKD materials owing to the presence of parasitic electrical resistances between the electrical contacts and SKD and the resistance of the electrical connection wires. The obtained S values for the SKD device are 8–20% higher than the average values for p-type and n-type SKD materials from both the ideal and the comprehensive models. However, the average power factor ($S^2\sigma$) values of the SKD device only deviate by 7% and 17% in comparison with the average values of p-type and n-type SKD materials from the comprehensive and the ideal models, respectively. The λ_{TE} values obtained for the SKD device are 50% and 100% higher than those of p-type and n-type SKD materials from the comprehensive and the ideal models, respectively; hence, the somewhat low ZT values of the SKD device (60% of the average value for p- and n-type SKD) in this study could be due to the high thermal conductivity values from the impedance spectra. This observation may be associated with variations in the thermoelectric properties of the SKD thermoelectric legs during device fabrication. It is necessary to conduct further studies

to verify the differences between the thermoelectric properties of devices and materials and understand the underlying fundamental properties of thermoelectric devices.
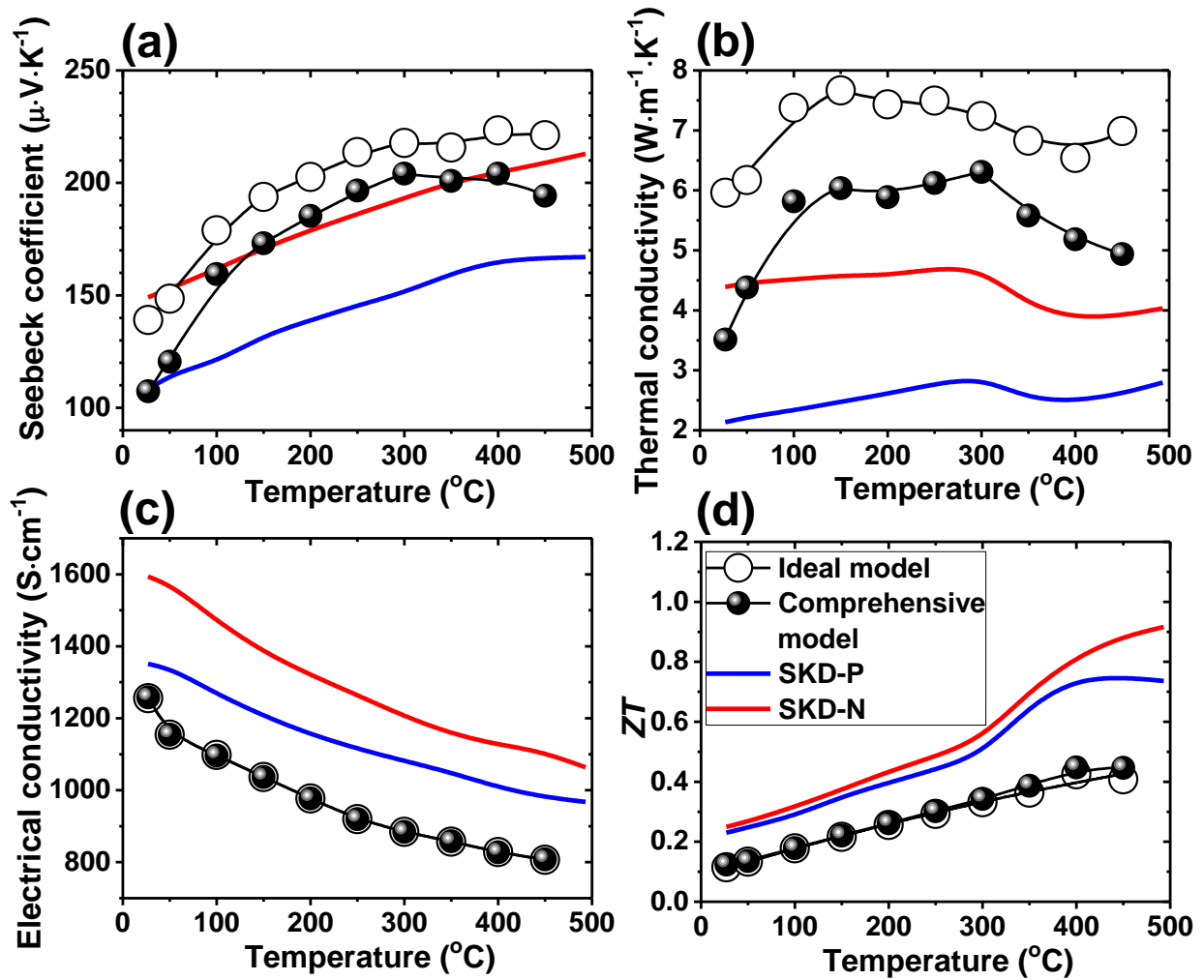
Fig. 9 Variations in (a) electrical conductivity (σ), (b) thermal conductivity (λ_{TE}), (c) Seebeck coefficient (S), and (d) figure of merit (ZT) of the two-couple SKD device as a function of temperature, as determined from the impedance spectra by employing the ideal and comprehensive models. For comparison, the properties of SKD materials, measured using ZEM-3 (Ulvac-Riko) and laser flash analysis (LFA 457, Netzsch) [24], are also displayed.

4. Conclusions

We have systematically investigated the thermoelectric properties of a skutterudite-based thermoelectric device using impedance spectroscopy in the temperature range 23–450 °C. Prior to the impedance spectroscopy measurements, the interface from the titanium metallized skutterudite joints was characterized by combining scanning and transmission electron microscopy with specific electrical contact resistance measurements. Intermetallic phases (titanium antimony and titanium cobalt antimony compounds), found at the interface between titanium and skutterudite owing to the interdiffusion of titanium and skutterudite during the spark plasma sintering process, exhibited a low specific contact resistance of 3–4.5 $\mu\Omega\cdot$cm^2. All impedance spectra of the skutterudite-based thermoelectric device were Kramers–Kronig-transformable, which enabled least-squares analysis using both the ideal and the comprehensive mathematical models. Both models were used to extract the figure of merit and three key parameters (Seebeck coefficient, thermal conductivity, and electrical conductivity) from the impedance spectra as a function of temperature. Both models yielded similar electrical conductivity and figure of merit values, whereas the comprehensive model estimated the Seebeck coefficients and thermal conductivity values more accurately than the ideal model. The figure of merit values for the skutterudite-based device were 60% lower than those of skutterudite materials, mainly because the thermal conductivity of the device was higher than that of the skutterudite materials, whereas the average power factor values of the device were close to those of the materials. These deviations may be associated with variations in the thermoelectric properties of the skutterudite thermoelectric legs during device fabrication. These encouraging results indicate that the impedance spectroscopy is a useful tool for investigating the properties of thermoelectric devices. Furthermore, this study provides an important opportunity

to advance the understanding of thermoelectric device property, which is valuable information

for the design and optimization of thermoelectric conversion system to achieve the best

performance for the real applications.

Acknowledgements

Declarations of interest: none

Glossary

DD, didymium

EDS, energy-dispersive X-ray spectroscopy

FIB, focused ion beam

KK, Kramers–Kronig

HAADF-STEM, high-angle annular dark-field scanning transmission electron microscopy

Mm, mischmetal

SAED, selected-area electron diffraction

SEM, scanning electron microscopy

SKD, skutterudite

SPS, spark plasma sintering

A, area of the thermoelectric legs

C_p, specific heat

D, thermal diffusivity

h_1, radiative heat loss of the thermoelectric legs

h_2, radiative heat loss at the internal surface of the Al_2O_3 plate

h_3, radiative and convective heat loss at the external surface of the Al_2O_3 plate

h_C, convective heat transfer coefficient at the external surface of the ceramic plate

I, current amplitude

J_0, zero-order Bessel function

J_1, first-order Bessel function

L, length of the thermoelectric element

L_C, length of the ceramic plate

N, number of thermoelectric couples

PP, Peltier power density

R_C, thermoelectric resistance induced by the ceramic layer

R_{TE}, thermoelectric resistance

R_Ω, ohmic resistance

r_0, thermoelectric leg radius

S, Seebeck coefficient

S_{ave}, average Seebeck coefficient

T, absolute temperature

Y_{SC}, spreading-constriction impedance

Z_{im}, imaginary part of the impedance

Z_{re}, real part of the impedance

Z_{Wa}, adiabatic Warburg element

Z_{WCT}, constant temperature Warburg element

ZT, figure of merit

α_{TE}, thermal diffusivity of the thermoelectric element

α_C, thermal diffusivity of the ceramic plate

ε, emissivity

λ, thermal conductivity

λ_C, thermal conductivity of the insulating ceramic plate

λ_{TE}, thermal conductivity of the thermoelectric element

η, filling factor

ρ, mass density

σ, electrical conductivity

σ_B, Stefan–Boltzmann constant

χ^2, goodness-of-fit parameter

ω, angular frequency

ω_C, characteristic angular frequency of thermal diffusion of ceramic materials

ω_{TE}, characteristic angular frequency of thermal diffusion of thermoelectric materials

References

[1]   Meroz O, Gelbstein Y. Thermoelectric $Bi_2Te_{3-x}Se_x$ alloys for efficient thermal to
        electrical energy conversion. Phys Chem Chem Phys 2018;20:4092–9.
        doi:10.1039/C7CP06176E.

[2]   Beeri O, Rotem O, Hazan E, Katz EA, Braun A, Gelbstein Y. Hybrid photovoltaic-
        thermoelectric system for concentrated solar energy conversion: Experimental realization
        and modeling. J Appl Phys 2015;118:115104. doi:10.1063/1.4931428.

[3]   Vizel R, Bargig T, Beeri O, Gelbstein Y. Bonding of Bi_2Te_3-Based Thermoelectric Legs
        to Metallic Contacts Using $Bi_{0.82}Sb_{0.18}$ Alloy. J Electron Mater 2016;45:1296–300.
        doi:10.1007/s11664-015-4003-2.

[4]   Guttmann GM, Gertner R, Samuha S, Ben-Ayoun D, Haroush S, Gelbstein Y.
        Thermoelectric and mechanical properties of Ag and Cu doped $(GeTe)_{0.96}(Bi_2Te_3)_{0.04}$.
        MRS Commun 2018;8:1292–9. doi:10.1557/mrc.2018.150.

[5]   Hazan E, Madar N, Parag M, Casian V, Ben-Yehuda O, Gelbstein Y. Effective Electronic
        Mechanisms for Optimizing the Thermoelectric Properties of GeTe-Rich Alloys. Adv
        Electron Mater 2015;1:1500228. doi:10.1002/aelm.201500228.

[6]   Gelbstein Y, Dashevsky Z, Dariel MP. Highly efficient bismuth telluride doped p-type
        $Pb_{0.13}Ge_{0.87}Te$ for thermoelectric applications. Phys Status Solidi – Rapid Res Lett
        2007;1:232–4. doi:10.1002/pssr.200701160.

[7]   Wang H, Hwang J, Snedaker ML, Kim I, Kang C, Kim J, Stucky GD, Bowers J, Kim W.
        High Thermoelectric Performance of a Heterogeneous PbTe Nanocomposite. Chem Mater

2015;27:944–9. doi:10.1021/cm5042138.

[8]   Sootsman JR, Chung DY, Kanatzidis MG. New and Old Concepts in Thermoelectric
        Materials. Angew Chemie Int Ed 2009;48:8616–39. doi:10.1002/anie.200900598.

[9]   Fitriani, Ovik R, Long BD, Barma MC, Riaz M, Sabri MFM, Said S, Saidur R. A review
        on nanostructures of high-temperature thermoelectric materials for waste heat recovery.
        Renew Sustain Energy Rev 2016;64:635–59. doi:10.1016/J.RSER.2016.06.035.

[10]   Gayner C, Kar KK. Recent advances in thermoelectric materials. Prog Mater Sci
        2016;83:330–82. doi:10.1016/J.PMATSCI.2016.07.002.

[11]   Zhu T, Liu Y, Fu C, Heremans JP, Snyder JG, Zhao X. Compromise and Synergy in High-
        Efficiency Thermoelectric Materials. Adv Mater 2017;29:1605884.
        doi:10.1002/adma.201605884.

[12]   Rogl G, Rogl P. Skutterudites, a most promising group of thermoelectric materials. Curr
        Opin Green Sustain Chem 2017;4:50–7. doi:10.1016/J.COGSC.2017.02.006.

[13]   Appel O, Schwall M, Mogilyansky D, Köhne M, Balke B, Gelbstein Y. Effects of
        Microstructural Evolution on the Thermoelectric Properties of Spark-Plasma-Sintered
        $Ti_{0.3}Zr_{0.35}Hf_{0.35}NiSn$ Half-Heusler Compound. J Electron Mater 2013;42:1340–5.
        doi:10.1007/s11664-012-2249-5.

[14]   He J, Tritt TM. Advances in thermoelectric materials research: Looking back and moving
        forward. Science 2017;357:eaak9997. doi:10.1126/science.aak9997.

[15]   Appel O, Zilber T, Kalabukhov S, Beeri O, Gelbstein Y. Morphological effects on the
        thermoelectric properties of $Ti_{0.3}Zr_{0.35}Hf_{0.35}Ni_{1+\delta}Sn$ alloys following phase separation. J

Mater Chem C 2015;3:11653–9. doi:10.1039/C5TC03214H.

[16] Wang H, McCarty R, Salvador JR, Yamamoto A, König J. Determination of Thermoelectric Module Efficiency: A Survey. J Electron Mater 2014;43:2274–86. doi:10.1007/s11664-014-3044-2.

[17] Kato K, Hatasako Y, Kashiwagi M, Hagino H, Adachi C, Miyazaki K. Fabrication of a Flexible Bismuth Telluride Power Generation Module Using Microporous Polyimide Films as Substrates. J Electron Mater 2014;43:1733–9. doi:10.1007/s11664-013-2852-0.

[18] Hu X, Jood P, Ohta M, Kunii M, Nagase K, Nishiate H, Kanazidis MG, Yamamoto A. Power generation from nanostructured PbTe-based thermoelectrics: comprehensive development from materials to modules. Energy Environ Sci 2016;9:517–29. doi:10.1039/C5EE02979A.

[19] Jood P, Ohta M, Yamamoto A, Kanatzidis MG. Excessively Doped PbTe with Ge-Induced Nanostructures Enables High-Efficiency Thermoelectric Modules. Joule 2018;2:1339–55. doi:10.1016/J.JOULE.2018.04.025.

[20] Nie G, Suzuki S, Tomida T, Sumiyoshi A, Ochi T, Mukaiyama K, Kikuchi M, Guo JQ, Yamamoto A, Obara H. Performance of Skutterudite-Based Modules. J Electron Mater 2017;46:2640–4. doi:10.1007/s11664-016-4849-y.

[21] Zhao D, Tian C, Tang S, Liu Y, Jiang L, Chen L. Fabrication of a $CoSb_3$-based thermoelectric module. Mater Sci Semicond Process 2010;13:221–4. doi:10.1016/J.MSSP.2010.10.016.

[22] Guo JQ, Geng HY, Ochi T, Suzuki S, Kikuchi M, Yamaguchi Y, ITO S. Development of

Skutterudite Thermoelectric Materials and Modules. J Electron Mater 2012;41:1036–42. doi:10.1007/s11664-012-1958-0.

[23]   Salvador JR, Cho JY, Ye Z, Moczygemba JE, Thompson AJ, Sharp JW, Koenig JD, Maloney R, Thompson T, Sakamoto J, Wang H, Wereszczak AA. Conversion efficiency of skutterudite-based thermoelectric modules. Phys Chem Chem Phys 2014;16:12510–20. doi:10.1039/C4CP01582G.

[24]   Park SH, Jin Y, Cha J, Hong K, Kim Y, Yoon H, Yoo CY, Chung I. High-Power-Density Skutterudite-Based Thermoelectric Modules with Ultralow Contact Resistivity Using Fe–Ni Metallization Layers. ACS Appl Energy Mater 2018;1:1603–11. doi:10.1021/acsaem.8b00064.

[25]   Zhang Q, Zhou Z, Dylla M, Agne MT, Pei Y, Wang L, Tang Y, Liao J, Li J, Bai S, Jiang W, Chen L, Snyder GJ. Realizing high-performance thermoelectric power generation through grain boundary engineering of skutterudite-based nanocomposites. Nano Energy 2017;41:501–10. doi:https://doi.org/10.1016/j.nanoen.2017.10.003.

[26]   Bartholomé K, Balke B, Zuckermann D, Köhne M, Müller M, Tarantik K, König J. Thermoelectric Modules Based on Half-Heusler Materials Produced in Large Quantities. J Electron Mater 2014;43:1775–81. doi:10.1007/s11664-013-2863-x.

[27]   Populoh S, Brunko O, Gałązka K, Xie W, Weidenkaff A. Half-Heusler (TiZrHf)NiSn Unileg Module with High Powder Density. Materials (Basel) 2013;6:1326–32. doi:10.3390/ma6041326.

[28]   Fu C, Bai S, Liu Y, Tang Y, Chen L, Zhao X, Zhu T. Realizing high figure of merit in

heavy-band p-type half-Heusler thermoelectric materials. Nat Commun 2015;6:8144.

doi:10.1038/ncomms9144.

[29] García-Cañadas J, Min G. Impedance spectroscopy models for the complete

characterization of thermoelectric materials. J Appl Phys 2014;116:174510.

doi:10.1063/1.4901213.

[30] Beltrán-Pitarch B, Prado-Gonjal J, Powell A V, Ziolkowski P, García-Cañadas J. Thermal

conductivity, electrical resistivity, and dimensionless figure of merit (ZT) determination of

thermoelectric materials by impedance spectroscopy up to 250 °C. J Appl Phys

2018;124:25105. doi:10.1063/1.5036937.

[31] Beltrán-Pitarch B, Prado-Gonjal J, Powell A V., García-Cañadas J. Experimental

conditions required for accurate measurements of electrical resistivity, thermal

conductivity, and dimensionless figure of merit (ZT) using Harman and impedance

spectroscopy methods. J Appl Phys 2019;125:025111. doi:10.1063/1.5077071.

[32] García-Cañadas J, Min G. Low Frequency Impedance Spectroscopy Analysis of

Thermoelectric Modules. J Electron Mater 2014;43:2411–4. doi:10.1007/s11664-014-

3095-4.

[33] Yoo C-Y, Kim Y, Hwang J, Yoon H, Cho BJ, Min G, Park SH. Impedance spectroscopy

for assessment of thermoelectric module properties under a practical operating

temperature. Energy 2018;152:834–9. doi:10.1016/J.ENERGY.2017.12.014.

[34] Beltrán-Pitarch B, Márquez-García L, Min G, García-Cañadas J. Measurement of thermal

conductivity and thermal diffusivity using a thermoelectric module. Meas Sci Technol

2017;28:045902. doi:10.1088/1361-6501/aa5c30.

[35]   Otsuka M, Hasegawa Y, Arisaka T, Shinozaki R, Morita H. Dimensionless figure of merit

and its efficiency estimation for transient response of thermoelectric module based on

impedance spectroscopy. Appl Phys Express 2017;10:115801.

doi:10.7567/APEX.10.115801.

[36]   Hasegawa Y, Otsuka M. Temperature dependence of dimensionless figure of merit of a

thermoelectric module estimated by impedance spectroscopy. AIP Adv 2018;8:075222.

doi:10.1063/1.5040181.

[37]   Mesalam R, Williams HR, Ambrosi RM, García-Cañadas J, Stephenson K. Towards a

comprehensive model for characterising and assessing thermoelectric modules by

impedance spectroscopy. Appl Energy 2018;226:1208–18.

doi:10.1016/J.APENERGY.2018.05.041.

[38]   Thiébaut E, Pesty F, Goupil C, Guegan G, Lecoeur P. Non-linear impedance spectroscopy

for complete thermoelectric characterization: Beyond the zT estimation. J Appl Phys

2018;124:235106. doi:10.1063/1.5063419.

[39]   Prado-Gonjal J, Phillips M, Vaqueiro P, Min G, Powell A V. Skutterudite Thermoelectric

Modules with High Volume-Power-Density: Scalability and Reproducibility. ACS Appl

Energy Mater 2018;1:6609–18. doi:10.1021/acsaem.8b01548.

[40]   Yoo C-Y, Yoon H, Park SH. Direct Comparison of Thermoelectric Devices Using

Impedance Spectroscopy. J Electron Mater 2018:1–7. doi:10.1007/s11664-018-6777-5.

[41]   Rogl G, Grytsiv A, Failamani F, Hochenhofer M, Bauer E, Rogl P. Attempts to further

enhance ZT in skutterudites via nano-composites. J Alloys Compd 2017;695:682–96. doi:https://doi.org/10.1016/j.jallcom.2016.10.114.

[42] Klinger M, IUCr. More features, more tools, more *CrysTBox*. J Appl Crystallogr 2017;50:1226–34. doi:10.1107/S1600576717006793.

[43] Kim Y, Yoon G, Park SH. Direct Contact Resistance Evaluation of Thermoelectric Legs. Exp Mech 2016;56:861–9. doi:10.1007/s11340-016-0131-8.

[44] Chen YQ. High-pressure synthesis and thermoelectric properties of Yb-filled skutterudite compounds. Muroran Institute of Technology, 2016.

[45] Zhao D, Li X, He L, Jiang W, Chen L. High temperature reliability evaluation of $CoSb_3$/electrode thermoelectric joints. Intermetallics 2009;17:136–41. doi:10.1016/j.intermet.2008.10.010.

[46] Fan J, Chen L, Bai S, Shi X. Joining of Mo to $CoSb_3$ by spark plasma sintering by inserting a Ti interlayer. vol. 58. 2004. doi:10.1016/j.matlet.2004.07.041.

[47] Zhao D, Geng H, Chen L. Microstructure Contact Studies for Skutterudite Thermoelectric Devices. Int J Appl Ceram Technol 2012;9:733–41. doi:10.1111/j.1744-7402.2011.02703.x.

[48] Gu M, Xia X, Li X, Huang X, Chen L. Microstructural evolution of the interfacial layer in the Ti–Al/$Yb_{0.6}Co_4Sb_{12}$ thermoelectric joints at high temperature. J Alloys Compd 2014;610:665–70. doi:10.1016/j.jallcom.2014.05.087.

[49] Gu M, Xia X, Huang X, Bai S, Li X, Chen L. Study on the interfacial stability of p-type Ti/$Ce_yFe_xCo_{4-x}Sb_{12}$ thermoelectric joints at high temperature. J Alloys Compd

2016;671:238–44. doi:10.1016/j.jallcom.2016.02.041.

[50]   Zhao D, Geng H, Chen L. Microstructure Contact Studies for Skutterudite Thermoelectric

       Devices. Int J Appl Ceram Technol 2012;9:733–41. doi:10.1111/j.1744-

       7402.2011.02703.x.

[51]   Boukamp BA. A Linear Kronig-Kramers Transform Test for Immittance Data Validation.

       J Electrochem Soc 1995;142:1885. doi:10.1149/1.2044210.

[52]   Boukamp BA. Electrochemical impedance spectroscopy in solid state ionics: recent

       advances. Solid State Ionics 2004;169:65–73. doi:10.1016/J.SSI.2003.07.002.

[53]   Hirschorn B, Orazem ME. On the Sensitivity of the Kramers–Kronig Relations to

       Nonlinear Effects in Impedance Measurements. J Electrochem Soc 2009;156:C345.

       doi:10.1149/1.3190160.

[54]   Beltrán-Pitarch B, García-Cañadas J. Influence of convection at outer ceramic surfaces on

       the characterization of thermoelectric modules by impedance spectroscopy. J Appl Phys

       2018;123:084505. doi:10.1063/1.5019881.

Supplementary Material
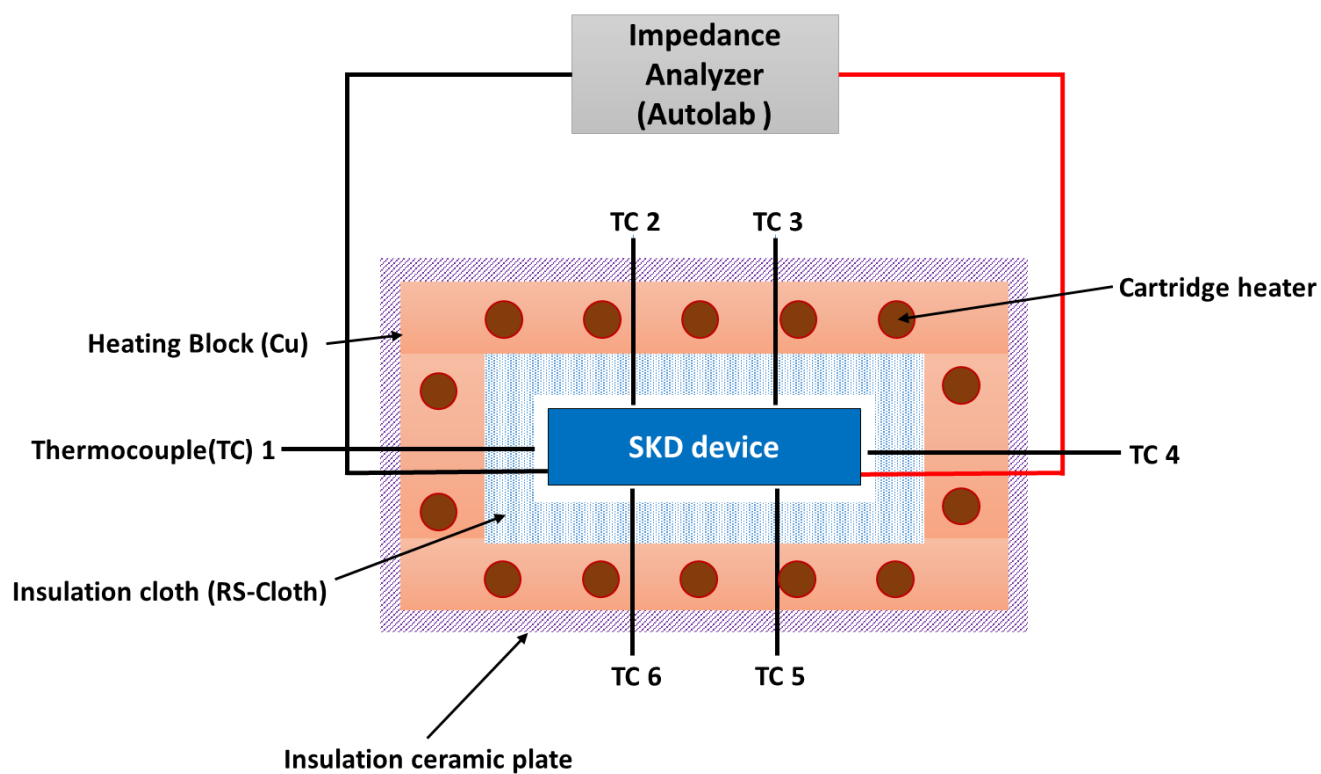
Determination of the thermoelectric properties of a skutterudite-based device at practical operating temperatures by impedance spectroscopy

Chung-Yul Yoo[a,*], Changho Yeon[a], Younghwan Jin[a], Yeongseon Kim[a], Jinseop Song[a], Hana Yoon[a], Sang Hyun Park[a], Braulio Beltrán-Pitarch[b], Jorge García-Cañadas[b], Gao Min[c]
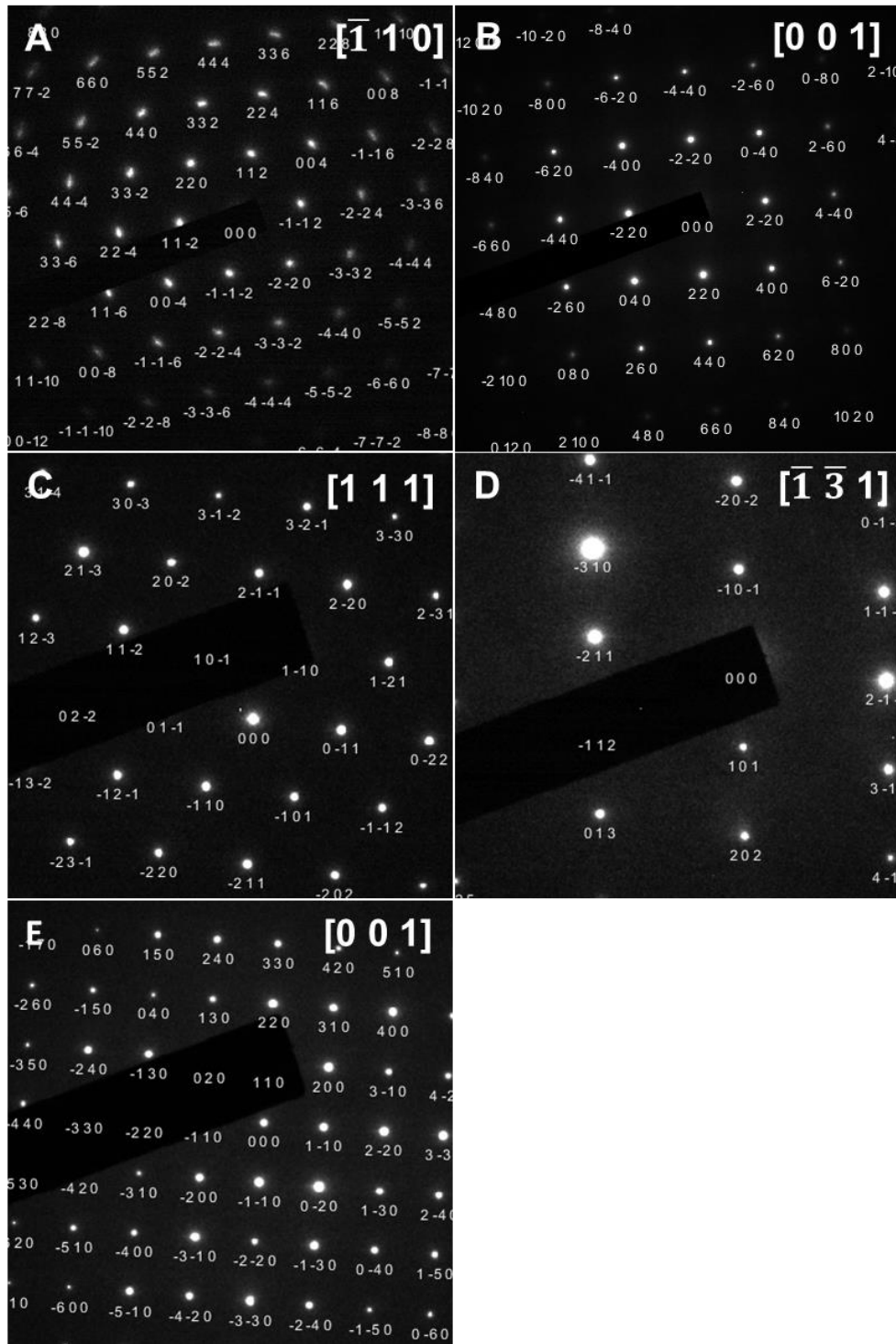
[a]Korea Institute of Energy Research, 152 Gajeong-ro, Yuseong-gu, Daejeon 34129, Republic of Korea

[b]Department of Industrial Systems Engineering and Design, Universitat Jaume I, Campus del Riu Sec, 12071 Castellón, Spain
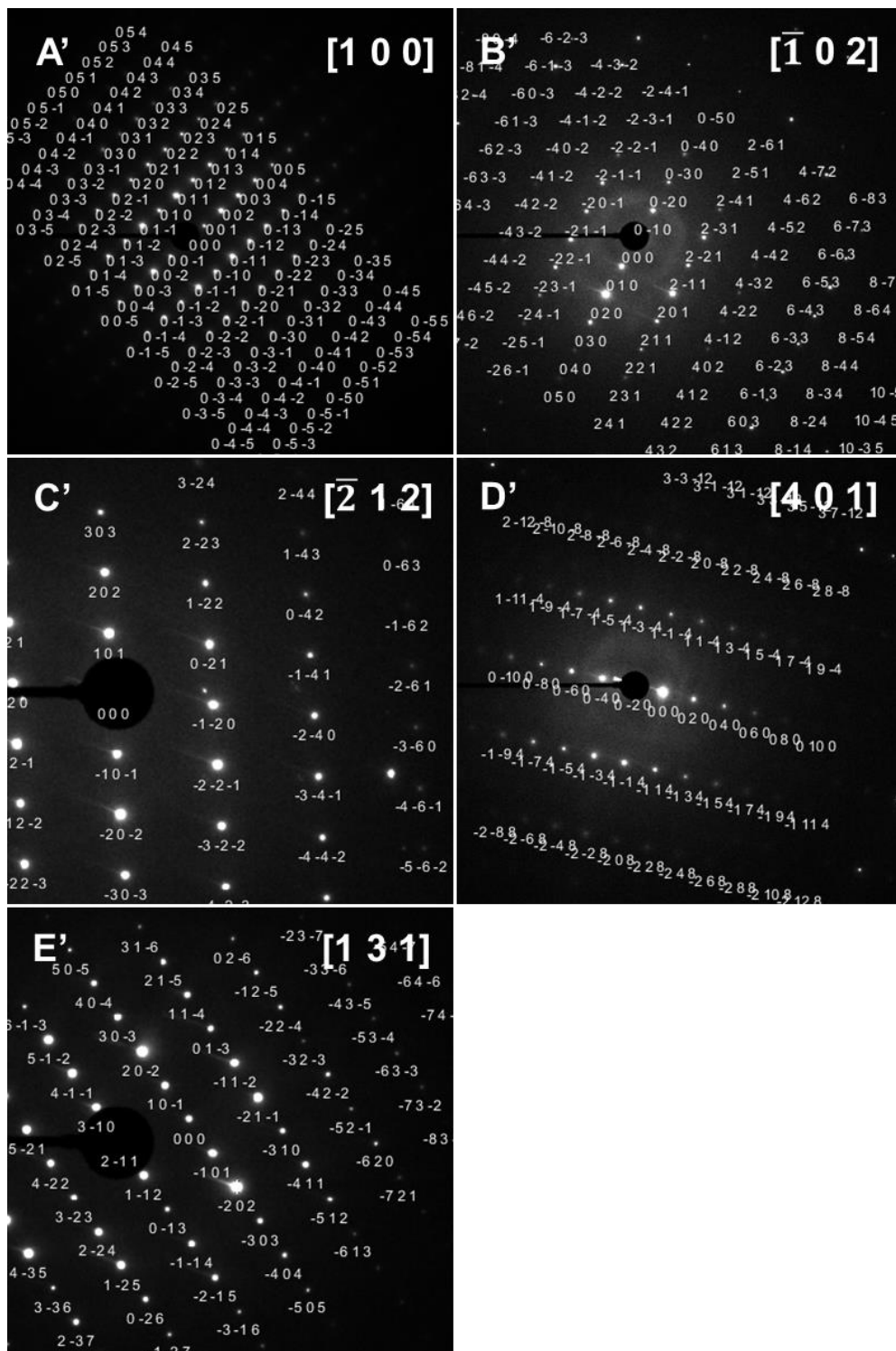
[c]School of Engineering, Cardiff University, Cardiff CF24 3AA, United Kingdom

Fig. S1 Schematic of experimental setup (side view).

Fig. S2 Indexing of the selected-area electron diffraction (SAED) patterns at the Ti/SKD interface for p-type SKD.

Fig. S3 Indexing of the selected-area electron diffraction (SAED) patterns at the Ti/SKD interface for n-type SKD.